Available online at www.sciencedirect.com
ScienceDirect
Geochimica et Cosmochimica Acta 73 (2009) 5377–5393
Geochimica et Cosmochimica Acta
www.elsevier.com/locate/gca

Quantification of initial steps of nucleation and growth of silica nanoparticles: An *in-situ* SAXS and DLS study

Dominique J. Tobler [a,*,1], Sam Shaw [a], Liane G. Benning [a]

[a] *Earth and Biosphere Institute, School of Earth and Environment, University of Leeds, LS2 9JT Leeds, UK*

Received 18 November 2008; accepted in revised form 2 June 2009; available online 14 June 2009

Abstract

The initial steps of silica polymerization and silica nanoparticle formation have been studied *in-situ* and in real-time. The experiments were carried out in near neutral pH (7–8) solutions with initial silica concentrations of 640 and 1600 ppm ([SiO_2]) and ionic strengths (IS) of 0.02, 0.05, 0.11 and 0.22 M. The polymerization reactions were induced by neutralizing a high pH silica solution (from pH 12 to 7) and monitored by the time-dependent depletion in monosilicic acid concentration over time. The accompanied nucleation and growth of silica nanoparticles (i.e., change in particle size over time) was followed *in-situ* using time-resolved synchrotron-based Small Angle X-ray Scattering (SAXS) and conventional Dynamic Light Scattering (DLS) combined with scanning and (cryo)-transmission electron microscopy (SEM/cryo-TEM).

The critical nucleus diameter was quantified (1.4–2 nm) and results from SAXS and DLS showed that over 3 h the particle diameter increased to a final size of ~8 nm. SEM and TEM photomicrographs verified the SAXS and DLS data and confirmed the spherical and hydrous structure of the forming silica nanoparticles. Furthermore, fractal analysis (i.e., fractal dimension, $D_m \sim 2.2$) indicated that the formed particles consisted of open, polymeric, low-density structures.

For the nucleation and growth of silica nanoparticles a 3-stage growth process is proposed: (1) homogeneous and instantaneous nucleation of silica nanoparticles, (2) 3-D, surface-controlled particle growth following 1st order reaction kinetics and (3) Ostwald ripening and particle aggregation.

1. INTRODUCTION

Silica polymerization and the subsequent formation of silica nanoparticles occur in many modern terrestrial environments (e.g., hot springs, brines, deep reservoirs) but they have also played an important role in ancient geological settings (e.g., most Archean fossils were preserved in silica cherts; Barghorn and Tyler, 1965; Knoll, 1985; Carson, 1991; Westall and Walsh, 2000). Furthermore, these processes are believed to have been crucial to the formation of silica-rich deposits recently observed on Mars (Squyres et al., 2008).

The processes and mechanisms controlling silica precipitation are essential to the understanding of natural processes such as sinter formation (Guidry and Chafetz, 2002; Mountain et al., 2003), biosilicification (Konhauser et al., 2004 and references therein), silica diagenesis (Rimstidt and Barnes, 1980; Williams and Crerar, 1985; Hinman, 1990), formation of diatoms (Perry and Keeling-Tucker, 2000 and references therein) and silica scaling in geothermal power developments (Gunnarsson and Arnórsson, 2003). The formation of silica nanoparticles is also important in industrial processes and applications (e.g., computer, biotechnology, catalysis and chromatography) where the specific structural properties of silica nanoparticles (e.g., swelling capacity, strength, durability, thermal stability) make them highly desirable nanomaterials. As a result, the synthesis of highly monodisperse, spherical silica particles through techniques such as the Stöber method (the base

* Corresponding author. Fax: +44 113 343 5259.
E-mail address: tobler@see.leeds.ac.uk (D.J. Tobler).
[1] Present address: NASA Goddard Space Flight Center, Greenbelt, MD 20771, USA.

0016-7037/$ - see front matter © 2009 Elsevier Ltd. All rights reserved.
doi:10.1016/j.gca.2009.06.002

catalyzed hydrolysis and condensation of silicon alkoxides in low-molecular-weight alcohols; Stöber et al., 1968) are well established for industrial processes and the mechanisms and kinetics underlying these processes have been studied extensively (see below). Multiple techniques such as Small Angle X-Ray Scattering (SAXS), Dynamic and Static Light Scattering (DLS, SLS), ^{29}Si NMR, Raman spectroscopy and Transmission Electron Microscopy have been applied to derive models that describe the formation of alkoxide based silica particles under a variety of reactants and catalysts concentrations (Bogush et al., 1988; Matsoukas and Gulari, 1988; Bailey and Mecartney, 1992; van Blaaderen et al., 1992; Boukari et al., 1997, 2000; Pontoni et al., 2002; Green et al., 2003a,b). Despite the plethora of research for industrial applications, the Stöber method is not representative of silica nanoparticle formation in natural environments and the derived models may therefore not be transferable.

The mechanism of silica nanoparticle formation in natural systems have also been widely investigated (Alexander, 1954; Goto, 1956; Baumann, 1959; Kitahara, 1960; Iler, 1979; Rothbaum and Rhode, 1979; Crerar et al., 1981; Weres et al., 1981; Carroll et al., 1998; Icopini et al., 2005; Conrad et al., 2007). Overall, it is accepted that silica polymerization and silica nanoparticle formation follows a 3-stage process where (1) silica polymerization and nucleation of silica nanospheres is followed by (2) particle growth and/or ripening and (3) particle aggregation. In the first stage, silica monomers polymerize via dimers, trimers, etc. to cyclic oligomers which then form 3-D internally condensed nanospherical particles. During the second stage the particles grow by further accretion of silica oligomers and/or by Ostwald ripening. However, in most natural waters colloidal silica particles are not stable within the polymerizing solution and they tend to aggregate (stage 3) before completion of the ripening process (Iler, 1979; Perry, 2003; Benning et al., 2005; Icopini et al., 2005).

The parameters that influence this 3-stage process include temperature (T), pH, ionic strength (IS) and initial silica concentration ($[SiO_2]$), i.e., degree of silica saturation (White et al., 1956; Baumann, 1959; Iler, 1979; Rothbaum and Rhode, 1979; Marshall and Warakomski, 1980; Weres et al., 1981; Marshall and Chen, 1982; Gunnarsson and Arnórsson, 2003; Icopini et al., 2005; Conrad et al., 2007). In some cases, an induction period can precede the polymerization reaction during which little or no silica polymerization takes place. The length of this induction period is controlled by the same factors that determine silica polymerization (i.e., T, pH, IS and $[SiO_2]$) and it decreases with increasing degree of supersaturation (White et al., 1956; Iler, 1979; Rothbaum and Rhode, 1979; Gunnarsson and Arnórsson, 2003; Icopini et al., 2005; Conrad et al., 2007).

So far few attempts were made to image and quantify the size of the nanoparticles forming within the polymerizing solution. Rothbaum and Rhode (1979) determined the relative size of silica nanoparticles using chromatography, viscosity measurements and light scattering and concluded that with increasing temperature (from 5 to 180 °C), the average molecular weight of the polymers formed increased from approximately 10^5 to 10^9. Makrides et al. (1980) used light scattering to follow the polymerization process and proposed a primary nuclei size in the order of a few angstroms, which towards the end of the reaction reached several nm in size. More recently, Icopini et al. (2005) and Conrad et al. (2007) used Atomic Force Microscopy (AFM) to image the nanoparticulate silica fraction grown for 12 h and suggested that the primary particles were about 3 nm in diameter. These data supported previous results by Iler (1979) who postulated that at pH 2–7 the silica particles are unlikely to grow larger than 2–3 nm.

However, none of these studies provide any direct evidence for the rates and mechanisms of silica nanoparticle formation and little to no quantitative or time-resolved data on the size of the nanoparticles forming within the polymerizing solution. In addition, despite the wide-ranging research efforts to elucidate the reaction mechanisms and rates of silica polymerization a molecular level mechanistic understanding of the first steps in the nucleation and growth of primary silica particles in natural aqueous solution is still lacking.

Here we present the first direct quantification of the initial steps of silica polymerization and silica nanoparticle formation in inorganic solutions that mimicked natural waters. The reaction progress (i.e., nucleation and growth of silica nanoparticles) was followed *in-situ* and in real-time using synchrotron-based Small Angle X-ray Scattering (SAXS) and conventional Dynamic Light Scattering (DLS) combined with electron microscopic techniques (Scanning and Transmission Electron Microscopy, SEM/TEM). A series of experiments were carried out at a range of silica concentrations and ionic strengths and a kinetic model was developed for the growth of silica nanoparticles divided into 3-stages: (1) nucleation of critical nuclei, (2) particle growth and (3) particle ripening and aggregation.

2. KINETIC STUDIES ON THE SILICA POLYMERIZATION PROCESS

In the last few decades a range of reaction kinetic models have been derived from the measurements of the time-dependent decrease in monosilicic acid concentration ($[SiO_2(aq)]$) with reaction orders ranging between 1 and 5 (Table 1). Note that the time length chosen for monitoring the decrease in $[SiO_2(aq)]$ varied significantly between the mentioned studies (1.5–3000 h, Table 1). Early studies by Alexander (1954), Goto (1956) and Okamoto et al. (1957) indicated that the reaction order was dependent on the solution pH, with a 2nd order rate dependence for silica condensation between pH 3 and 7 and a third order rate dependence for pH > 7 and pH < 3 (Table 1). These results agreed with observations made by Kitahara (1960). In contrast, Baumann (1959) proposed that during silica polymerization the reaction order varied between 1 and 5 as a function of both initial silica concentration and pH.

Most of these reaction orders were determined by fitting the time-dependent depletion of $[SiO_2(aq)]$ in the reacting solution to a rate equation originally used by Goto (1956) (Table 1).

Table 1
Summary of reported experimentally derived kinetic models for the decrease in monosilicic acid concentration during the process of silica polymerization.

Study	PH	T (°C)	[$Si0_2$] (ppm)	Max. reaction time (h)	[a]Reaction order, n
Alexander (1954)	1–6	1.9	6000	170	3 for pH < 3.2 2 for pH > 3.2
Goto (1956), Okamoto et al. (1957)	7–10	22.3	200–900	144	3
Baumann (1959)	0.5–9	30	400–4000	7	1 to 5
Kitahara (1960)	3–10	0–100	500–800	5	2 for pH < 7.5 3 for pH > 7.5
Bishop and Bear (1972)	8.5	25–45	300	200	2
Rothbaum and Wilson (1977)	7.8–8.7	50–120	500–1000	1000	5–8
Rothbaum and Rhode (1979)	7–8	5–180	300–1300	1200	4
Makrides et al. (1977,1980)	4.5–6.5	75–105	700–1200	22	[c]0
[b]Peck and Axtmann (1979)	4.5–8.5	25–95	400–1000		1
[d,e]Weres et al. (1981)	2.5–8	50–100	500–1200	1.5	1 for $S > S_t$ 5 for $S < S_t$
Crerar et al. (1981)	7	25	1000	22	1
Icopini et al. (2005), Conrad et al. (2007)	3–11	25	250–1250	3000	4

[a] Reported rate laws were derived via the equation $-dC/dt \sim k(C - C_s)^n$ following the method described by Goto (1956).
[b] Peck and Axtmann (1979) analysed experiments reported by Makrides et al. (1980) and Rothbaum and Wilson (1977).
[c] Makrides (1977, 1980) postulated that particle growth preceding the induction and nucleation phase was linear with time.
[d] Weres et al. (1981) used the same model as proposed by Makrides et al. (1977,1980) and Peck and Axtmann (1979).
[e] Weres et al. (1981) proposed a 5th order rate law up to a certain silica concentration, S_t, and a 1st order rate law above S_t.

More recent studies (Peck and Axtmann, 1979; Rothbaum and Rhode, 1979; Crerar et al., 1981; Weres et al., 1981; Icopini et al., 2005; Conrad et al., 2007) have successfully described the complete polymerization process with a single kinetic model (i.e., with no variation in reaction order with pH), yet the results of these studies disagree on the order of the reaction (Table 1). Peck and Axtmann (1979) proposed a first order reaction with respect to [SiO_2(aq)] and a dependency on the total surface area of the growing particles. Furthermore, they postulated that towards the later stages of silica polymerization, the reaction may be limited by monomer diffusion to the particle surface. Crerar et al. (1981) supported these findings but indicated that the end of the reaction was not diffusion-limited as proposed by Peck and Axtmann (1979) and instead was characterized by ripening. Interestingly, Rimstidt and Barnes (1980) have successfully employed a first order reaction model to both silica precipitation as well as silica dissolution. In contrast, other studies postulated reaction orders higher than 1 (Table 1). Rothbaum and Rhode (1979) investigated the effect of temperature (between 5 and 180 °C) and pH (7–8) on the kinetics of silica polymerization and showed that, after an initial induction time, the maximum reaction rate had a fourth order dependence relative to the normalized monosilicic acid concentration. Similar, Icopini et al. (2005) and Conrad et al. (2007) reported a fourth order decrease of [SiO_2(aq)] over time (Table 1) and showed that the rate constant was linearly dependent on solution pH.

The plethora of reported reaction models for the kinetics and mechanisms of silica formation demonstrates that silica polymerization reactions maybe too complex to be described by a single equation. It is also possible that different mechanisms of polymerization and particle formation operate under different physico-chemical conditions and time scales which can be further complicated by the occurrence of an induction period. Therefore, in order to obtain a full understanding of this process, a molecular approach that combines the changes in [SiO_2(aq)] with the quantification of the growing silica particles is needed.

3. METHODOLOGY

3.1. Silica nanoparticle synthesis

The nucleation and growth of silica nanoparticles was followed in aqueous solutions with initial silica concentrations ([SiO_2]) of 640 and 1600 ppm and at three different ionic strengths (IS) each. High pH stock solutions (~pH 12) of aqueous SiO_2 at the desired ionic strength were prepared by dissolving specific amounts of $Na_2SiO_2{\cdot}5H_2O$ and NaCl in 250 ml distilled water. Silica polymerization and silica nanoparticle formation were induced by adjusting the high pH solution to 7 using 1 M HCl. Data acquisition started immediately after the pH stabilized at 7 (usually within 5 min) and all reactions were carried out at 25 ± 2 °C. The length of each experiment varied between 1 and 3 h. The pH of the reacting solution was automatically recorded (at 5 min time intervals) via a pH meter (Orion 710 with a gel electrode) interfaced with a computer. In all experiments, the pH increased by 0.5–0.8 pH units.

Concomitant with the polymerization process, the decrease of monosilicic acid concentration, [SiO_2(aq)], was analysed over a time period of 3 h. A few milliliters of the reacting solution were removed after specific time steps and each aliquot was analysed for monosilicic acid and total silica concentration using the spectrophotometric molybdate yellow method (Greenberg et al., 1985).

3.2. Small Angle X-ray Scattering (SAXS) procedure

All SAXS measurements were carried out on the Dutch–Belgian beamline (DUBBLE) BM26 at the European Synchrotron Radiation Facility (ESRF), Grenoble, France. Here, we only detail the parameters that affected the data collection in this study and the full DUBBLE configuration and an example of Dubble data can be found in Borsboom et al. (1998) and Bras et al. (2003). A wavelength of 1 Å and a sample-to-detector distance of 3.5 m were used. Data were collected with a 2-D multiwire proportional detector (gas-filled and equipped with a CCD-camera -Photonic Science Xios-II) and a pair of ion chambers (positioned pre- and post-sample) that monitored the incoming and transmitted beam intensities, respectively. The q-axis was calibrated with the scattering pattern of wet rat-tail collagen.

SAXS experiments were carried out in flow-through mode to ensure that the solutions were well mixed at all times (Fig. 1A). The initial high pH silica solutions were prepared in a plastic beaker that was connected to both ends of a quartz capillary SAXS cell (1.5 mm outer diameter and 10 μm walls) via Teflon tubing. The solution in the beaker was continuously stirred and just prior to commencement of the SAXS data acquisition the pH of the initial solution was adjusted to 7. The pH adjusted solutions were circulated via a peristaltic pump from the beaker through the quartz capillary of the SAXS cell and back into the beaker (Fig. 1A).

Time-resolved SAXS spectra from the polymerizing silica solution were collected every 5 min over time periods between 1 and 3 h. Data-reduction (i.e., correction for detector alinearities, decaying ion beam – using the post-sample ion chamber values, and background scattering) as well as sector integration to convert the 2D to 1D SAXS patterns were carried out using XOTOKO and BSL (software packages from the Synchrotron Radiation Source, Daresbury Laboratory, UK), respectively. The reduced data were analysed using GNOM, an indirect transform program for SAXS data processing (Svergun, 1992). In the case of a dilute, monodisperse system GNOM evaluates a distance distribution function, $p(Rg)$, and provides an estimate for the radius of gyration, Rg (a shape independent radius). For spherical particles, $p(Rg)$ should be Gaussian-shaped (Svergun and Koch, 2003) and Rg is given by the apex of the $p(Rg)$ curve. GNOM also calculates I_0 which is the intensity at $q = 0$ (i.e., a direct measure of the electron density contrast and the total scattering volume; Glatter and Kratky, 1982) and an error of the fit.

3.3. Dynamic Light Scattering (DLS)

All DLS measurements were performed at room temperature (25 ± 2 °C), with a Zetasizer Nano ZS (Malvern Instruments) equipped with a He–Ne laser ($\lambda = 633$ nm) and a backscatter detector at a fixed angle of 173°. The instrument recorded the intensity autocorrelation function, which was transformed into volume functions to obtain size information.

DLS experiments were carried out using a flow-through system (Fig. 1B) similar to the one described above for the SAXS experiments. Teflon tubing was connected to a disposable plastic cuvette (stationary in the DLS instrument) and to a plastic beaker from which the constantly stirred and pH adjusted solutions were pumped through the cuvette using a peristaltic pump (Fig. 1B). In contrast to the SAXS experiments, the continuous flow was stopped during the recording of each DLS pattern (5 min/pattern and 30 s delay time in between to exchange solution) in order to avoid interferences with the data acquisition. Time-resolved DLS experiments were run up to 3 h using the same [SiO_2] and IS conditions as for the SAXS experiments. Despite the low data accuracy of DLS (errors can reach 40% at small particle sizes), this method was used to verify results obtained from SAXS. Furthermore, DLS is far more sensitive to the presence of aggregates as compared to SAXS and therefore it was appropriate for monitoring the beginning of aggregation processes.

3.4. Electron microscopy

Silica nanoparticles were imaged using field emission gun scanning electron microscopy (FEG–SEM), transmission electron microscopy (TEM) and high-resolution cryo-TEM. For FEG–SEM, samples were prepared by filtering a few milliliters of the polymerizing solution at specific time intervals through 0.1 μm polycarbonate filters, which were immediately washed with distilled water to remove the remaining salt and silica solution and left to dry at ambient temperatures. The filter papers were placed on SEM Al-stubs, coated with 3 nm of platinum and analysed

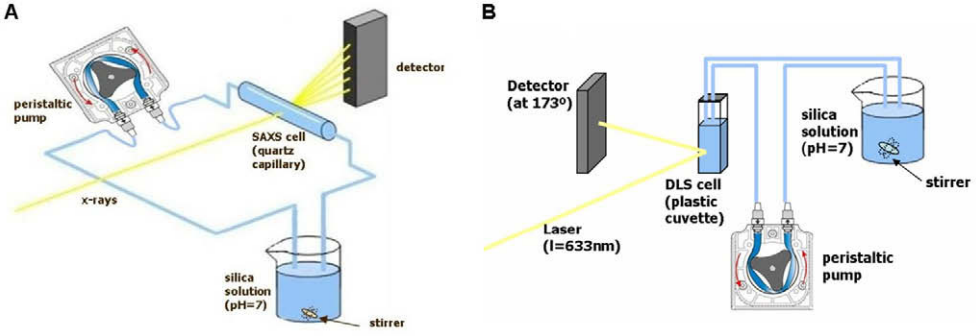

Fig. 1. Schematic illustration of continuous flow-through set-up of (A) SAXS and (B) DLS experiments.

with a LEO 1530 FEG–SEM using a working distance of 3 mm and a beam intensity of 3 kV. TEM samples were prepared by depositing a droplet of the reacting solutions on formvar coated copper grids. The grids were air dried and imaged using a Philips CM10 TEM at an accelerating voltage of 80 kV.

One sample was also imaged using a high-resolution cryo-TEM combined with an ultra-rapid freezing technique. In order to prepare the cryo-TEM samples, 5 μL of the reacting solution was deposited on a TEM grid which was then flash-frozen in liquid ethane (Egelhaaf et al., 2000) using a standard guillotine plunging device (vitrobot) that instantaneously vitrified the sample and avoided ice formation. The vitrified specimen was transferred at −180 °C onto a Gatan 626 cryo-holder and into a FEI T20FEG TEM operated at 200 kV. After an equilibration time of 1 h (until no apparent drift was observed), the specimen was examined at −180 °C and low dose images were recorded on a 4 × 4 k Gatan CCD-camera.

The size distributions of the silica particles were determined from the recorded images (both SEM and TEM). To obtain a size distribution with reasonably high precision, about 100–200 particles were measured in each image and the mean values and standard deviations were calculated.

3.5. Kinetic data analysis

For the kinetic analysis of the nucleation and growth of silica nanoparticles, the time-resolved SAXS data was tested against two particle nucleation and growth models: (a) the Chronomal kinetic model (Nielsen, 1964) and (b) the Johnson–Mehl–Avrami–Kolmogorov (JMAK) kinetic model (Avrami, 1939, 1940; Johnson and Mehl, 1939).

3.5.1. Chronomal kinetic model

If precipitation proceeds as a single rapid nucleation event followed by crystal growth it is possible to use the technique of Chronomal analysis (Nielsen, 1964) to determine the growth kinetics. The extent of crystallization is described by a fractional conversion, α, and the rate of crystallization by the linear rate of crystal growth, G:

$$G = \frac{dRg}{dt} = k(S_R - 1)^m \tag{1}$$

where Rg is the radius of gyration, m is the order of the growth process, k is the rate constant and S_R is the saturation ratio which is defined as $S_R = SI^{1/v}$ where SI is the saturation index and v is the stoichiometric coefficient (i.e., the sum of the stoichiometry of the products in the solubility expression). The SI values were calculated using the geochemical code PHREEQC (version 2.13.3; Parkhurst and Appelo, 1999) and the wateq4 database (Ball and Nordstrom, 1992) with the amorphous silica data updated using the values from Gunnarsson and Arnórsson (2000).

The fractional conversion and size of the crystal can be related by

$$\alpha = \left(\frac{Rg_t}{Rg^{max}}\right)^3 \tag{2}$$

where Rg_t is Rg at a given time t, and Rg^{max} is Rg at the end of the reaction, i.e., the final crystal size. Combining these relationships with a mass balance yields

$$\frac{d\alpha}{dt} = \frac{\alpha^{2/3}(1-\alpha)^m}{\tau} \tag{3}$$

where the time constant, τ, is related to the initial rate of growth, G_0, and the final crystal size, Rg^{max}:

$$\tau = \frac{Rg^{max}}{3G_0} \tag{4}$$

Eq. (3) can be integrated to give

$$I_m(\alpha) = \frac{t - t_0}{\tau} \tag{5}$$

where t_0 is the time of nucleation and I_m is the Chronomal function. We can define the inverse Chronomal function I_m^{-1}, so that $I_m^{-1}(I_m(\alpha)) = \alpha$ to give:

$$\left(\frac{Rg}{Rg^{max}}\right)^3 = I_m^{-1}\left(\frac{t - t_0}{\tau}\right) \tag{6}$$

The GNOM derived growth profiles (Rg *vs.* time) were fitted to Eq. (6) using three different types of reaction mechanisms (chemical, surface, or diffusion controlled) and varying reaction orders in order to obtain the best fit in terms of a regression coefficient, R_r^2. From the best fit, information about the critical nuclei radius, R_0, (by extrapolating to $t = 0$) and the initial growth rate, G_0 (s^{-1}), can be obtained.

3.5.2. The JMAK kinetic model

The JMAK model is based on the Avrami equation (Avrami, 1939):

$$\alpha = 1 - e^{-(k^*(t-t_o))^n} \tag{7}$$

where α is the degree of the reaction, t_0 is the initial time, k^* is the reaction constant and n is a constant related to the nucleation mechanism (i.e., instantaneous, decreasing rate, or constant rate), growth dimensionality (i.e., 1, 2, or 3-D) and reaction mechanism (i.e., diffusion- or surface-controlled; Hulbert, 1969).

To obtain α, Rg values from the SAXS data were normalized using Eq. (2). Both k^* and n can then be determined from the intercept and slope, respectively, of a $\ln(-\ln(1-\alpha))$ *vs.* $\ln t$ plot of the experimental data.

4. RESULTS

4.1. Time evolution of monosilicic acid concentration

The decrease of monosilicic acid concentration, [SiO_2(aq)], was monitored over 3 h in aqueous solutions with 640 and 1600 ppm SiO_2 and varying IS (Fig. 2). In the experiments with high initial silica concentration (Fig. 2, open symbols), about 80% of [SiO_2(aq)] (with respect to silica solubility at 25 °C; dotted line in Fig. 2) polymerized within the first 5 min, whereas only 15% of [SiO_2(aq)] was removed at the lower concentration (Fig. 2, full symbols). This showed that the initial silica concentration had a major impact on the rate of silica polymer-

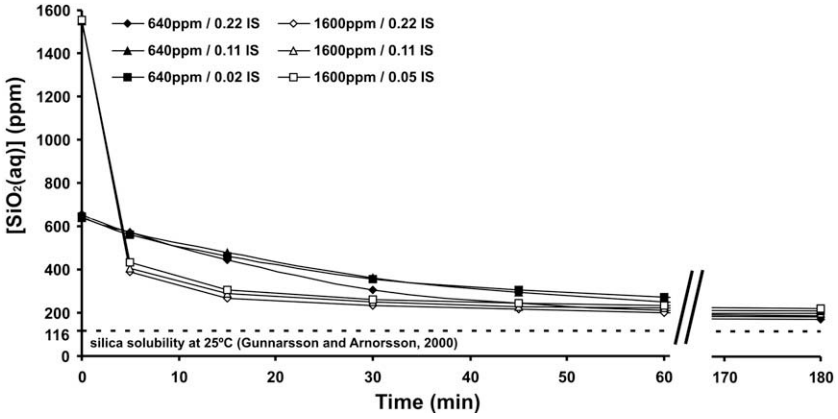

Fig. 2. Time-dependent depletion of monosilicic acid, [SiO_2(aq)], in solutions with 640 and 1600 ppm SiO_2 and IS of 0.02, 0.05, 0.11 and 0.22 (at pH 7). Note that the errors (<6%) are about the size of the symbols.

ization. In contrast, ionic strength seemed to have had less of an effect on the overall decrease of [SiO_2(aq)] over time, nevertheless solutions with higher IS exhibited slightly higher polymerization rates. In all data sets, a steady state close to the silica equilibrium solubility was obtained after only 3 h (Fig. 2).

Note that after 5 min, for all experiments with high initial SiO_2 concentration (1600 ppm), the monosilicic acid concentration had dropped significantly lower (~28%) than in the experiments at lower concentration (640 ppm SiO_2, Fig. 2). It is only after approximately 60 min that similar [SiO_2(aq)] values were established for all studied [SiO_2] and IS conditions. The fact that the rate of [SiO_2(aq)] depletion (as a function of time) is not identical between the two tested concentration regimes indicates that the polymerization reaction cannot be described by a simple chemical kinetic model, i.e., the reaction rate is not solely governed by silica concentration but also affected by other parameters (e.g., surface area of forming particles, pH).

4.2. SAXS

In Fig. 3, the log–log plot of a typical time-resolved SAXS profile from an experiment with 640 ppm SiO_2 and IS = 0.11 is shown. Note that in this experiment SAXS patterns were collected every 5 min over a time length of 155 min but for clarity only a few patterns are shown. The solid lines depict the GNOM fits, demonstrating both the quality of the SAXS data and the suitability of the GNOM model applied to the current data. The two dominant features in these plots were (i) the change in scattering intensity, $I(q)$ with time and (ii) the increase in the slope at low-q (i.e., Guinier region defined by $qRg < 1$; Guinier, 1939). The increase in $I(q)$ at low q is related to a change in electron density contrast between the matrix and the newly formed particles and a change in the total scattering volume (i.e., increase in particle volume or number) whereas the increase in the slope indicates an increase in the particle size with time.

The log–log plot also showed that the chosen system was sufficiently dilute (i.e., to make the analysis described above appropriate for the data), as indicated by the absence of a sharp increase or decrease in the scattering intensity at low q (Glatter and Kratky, 1982; Fig. 3).

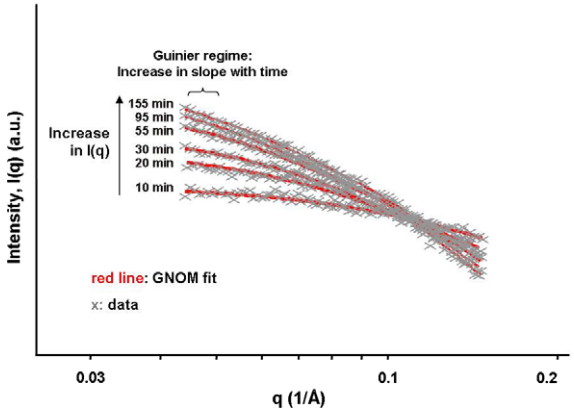

Fig. 3. Log–log plot of the scattering intensity as a function of scattering angle and time (640 ppm SiO_2, 0.11 IS). Note that SAXS profiles for the other data sets (i.e., low/high [SiO_2] or low/high IS) exhibited similar characteristics. Solid lines depict GNOM fits. For clarity, the errors for individual SAXS measurements (<3%) are not shown.

The radius of gyration, Rg, was evaluated from the full scattering pattern using GNOM and the assumption of a monodisperse distribution of spherical particles. The particle radius, R, was then evaluated from the following equation (valid for a sphere; Guinier, 1939):

$$Rg^2 = \frac{3}{5}R^2 \tag{8}$$

The time evolutions of the radius of a spherical silica particle, R, as a function of different [SiO_2] and IS are shown in Fig. 4A and B. In these plots, time = 0 min denotes the point where silica polymerization was initiated (i.e., pH adjusted to 7). It should be noted that no SAXS data could be obtained for the initial 10 min due to the experimental setup (i.e., ~5 min to stabilize pH at 7, securing the hutch and start experiment) and the time needed to acquire the first data point (i.e., 5 min).

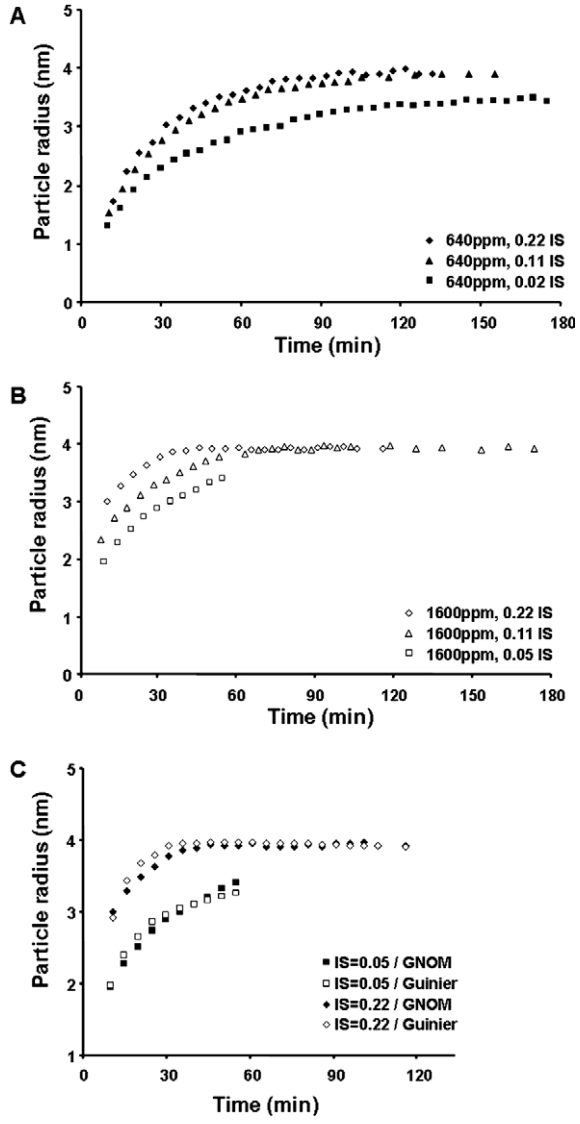

Fig. 4. Time evolution of particle radius showing the growth of silica nanoparticles in solutions with (A) 640 ppm and (B) 1600 ppm SiO_2 at three different IS each. Note that the errors (from GNOM fitting) were typically <3%, i.e., smaller than the symbols. (C) Comparison of R obtained from the GNOM and Guinier analysis (assuming spherical, monodisperse particles; text and Eq. (8)) for solutions with 1600 ppm SiO_2 and IS = 0.05 and 0.22.

For all tested [SiO_2] and IS conditions, the radius of the particles increased from about 1.5 (at low [SiO_2]) and ~3 nm (at high [SiO_2]) to ~4 nm (both concentration regimes) over 3 h confirming the growth of the particles (Fig. 4A and B). As expected from the time evolution of the monosilicic acid concentration (Fig. 2), the growth rate of the silica nanoparticles was enhanced in solutions containing higher initial silica concentrations (Fig. 4A and B). At 1600 ppm SiO_2, a final radius of ~4 nm was reached after only ~40 min (at high IS), while at the lower concentration (640 ppm SiO_2, high IS), the same radius was reached after only about 95 min. From the SAXS data it was evident that IS had a more pronounced effect on particle growth rate when compared to the time-dependent depletion of [SiO_2(aq)] (Fig. 2). For both tested silica concentrations, the growth rate was significantly higher in solutions with high IS (0.22) than with low IS (0.02 and 0.05, respectively) confirming the relationship between silica polymerization and IS (Marshall and Warakomski, 1980; Marshall and Chen, 1982). Despite differences in the apparent reaction rates, no induction times were observed on the time scales recorded.

Alternatively, Rg can be determined from the Guinier analysis in which Rg is evaluated from a plot of log $I(q)$ *vs.* q^2, known as the Guinier plot (Guinier, 1939). The slope of the linear region found in the low q range (Fig. 3, $qR\text{g} < 1$) determines Rg which can then be used to determine R of a sphere using Eq. (8). The comparison between R values calculated by the GNOM analysis and R extracted from the Guinier region (Fig. 4C) showed a good agreement between the two methods. However, R values determined using the Guinier approximation are very susceptible to errors introduced by selecting the Guinier region (i.e., low-q range for each SAXS pattern). In contrast, the GNOM code fits the whole scattering curve to obtain R and therefore all R values used for further calculations were evaluated using the GNOM code.

Fig. 5A shows the reaction progress, α_r, for all experiments where a final particle size, i.e., the end of particle growth, was reached (Fig. 4). α_r was determined from the changes in the scattering volume, I_0, of the growing particles over time using the following equation: $\alpha_r = I(t)/I_{max}$ where $I(t)$ is I_0 at a given time, and I_{max} is I_0 at the end of the reaction. Similar to the particle growth profiles (Fig. 4), the reactions proceeded fastest in solutions with the highest [SiO_2] and IS, as demonstrated by the fast increase in α_r at the beginning of the reaction and the early completion of the reaction ($\alpha_r = 1$).

An example of a time-resolved distance distribution function, $p(R)$, for a polymerizing solution with 1600 ppm SiO_2 and IS = 0.05 is shown in Fig. 5B. Over time, the $p(R)$ plot showed an increase in both the area under the curve and a shift in the apex of the curve indicating an increase in particle size. In the case of perfect, monodispersed spheres (a valid assumption for silica nanoparticles), the shape of each individual $p(R)$ curve should be Gaussian. Despite the $p(R)$ being slightly right-skewed, the near-Gaussian shape of the $p(R)$ curves obtained in this study (Fig. 5B) supported this assumption. The observed tail could be induced by the presence of a few aggregates or it could also indicate the presence of some degree of polydispersity. Note that the overall shape of the $p(R)$ curves did not differ between experiments (i.e., over the studied [SiO_2] and IS conditions) suggesting that the shape and the degree of polydispersity of the growing particles did not change between experiments.

4.3. DLS

The time-dependent growth of silica nanoparticles was monitored in six different solutions by DLS (Fig. 6, for clarity only four data sets are shown). Note that DLS measures

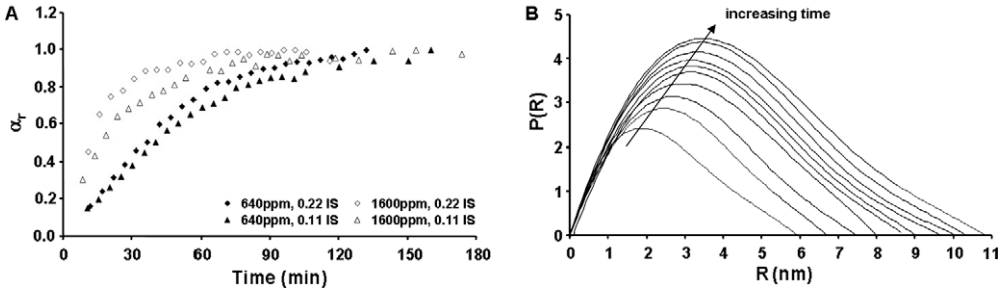

Fig. 5. (A) Time evolution of the normalized scattering intensity, α_r, in solutions with 640 and 1600 ppm SiO_2 at two different IS each. (B) $P(R)$ of scattered silica nanoparticles as a function of R and time ($t = 10$–55 min with time steps of 5 min) evaluated with GNOM and Eq. (8) (1600 ppm SiO_2, IS = 0.05).

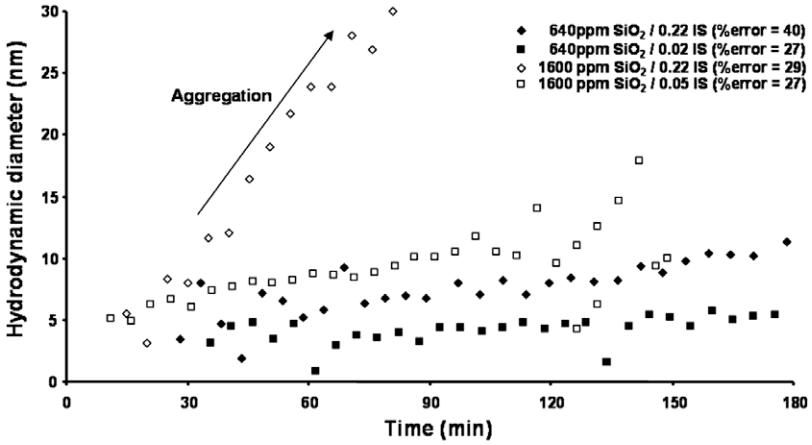

Fig. 6. Growth of silica nanoparticles in solutions with varying [SiO_2] and IS as determined by DLS. The arrow indicates the start of particle aggregation for solutions with 1600 ppm SiO_2 and IS of 0.22 (% errors are average values).

the time-dependent change in the apparent mean hydrodynamic diameter of the growing particles via changes in the scattering of laser light caused by the Brownian motion of the particles. In contrast to the SAXS measurements, the data showed large variations between single data points. Furthermore, due to the lower resolution of DLS at small particle sizes the average% error of the individual DLS data points ranged between 27 and 40 (Fig. 6). Despite these larger errors, overall, the trends between particle growth profiles and [SiO_2]/IS were similar to those observed with SAXS. However, the DLS growth curves differed from the SAXS results in two ways: (i) the appearance of the first detectable particle was delayed at lower [SiO_2] (~30 min; Fig. 6, full symbols) and (ii) following an initial steady growth a sudden increase in particle size was observed for higher concentrated solutions (Fig. 6; after 30 min for 1600 ppm SiO_2/0.22 IS). The observed delay at low concentrations probably represents an artefact of the lower detection limits of the DLS as compared to synchrotron-based SAXS measurements (~1 *vs.* 0.1 nm). Conversely, the dramatic increase in growth probably indicates aggregation as even a small percentage (1–2 vol%) of larger particles in a particle suspension would dramatically increase the overall particle diameter derived by DLS (www.malvern.com, technical note).

4.4. Electron microscopy

To image and verify the size of silica nanoparticles evaluated with SAXS and DLS, samples of the reacting solutions were removed after specific time steps (between 10 min and 3 h) for SEM and TEM analysis. Fig. 7A shows a FEG–SEM photomicrograph of silica nanoparticles after 30 min of polymerization in a solution with 1600 ppm SiO_2 and IS = 0.22. The particles are all aggregated but from image analyses an approximate particle diameter of 4–8 nm could be estimated for the individual particles within the aggregates.

A more accurate estimate of the particle size distributions was derived from the TEM photomicrographs (Fig. 7B) where the individual particles could be distinguished. The micrographs supported that the particles are approximately spherical and monodisperse. Using the TEM photomicrographs, the average particle diameter and the standard deviations (i.e., polydispersity) were determined for a variety of experimental conditions. The results are listed in Table 2 along with the results from DLS and SAXS (R values from SAXS were converted to particle diameter).

To test for artefacts caused by sample dehydration and the high vacuum of standard SEM and TEM analytical ap-

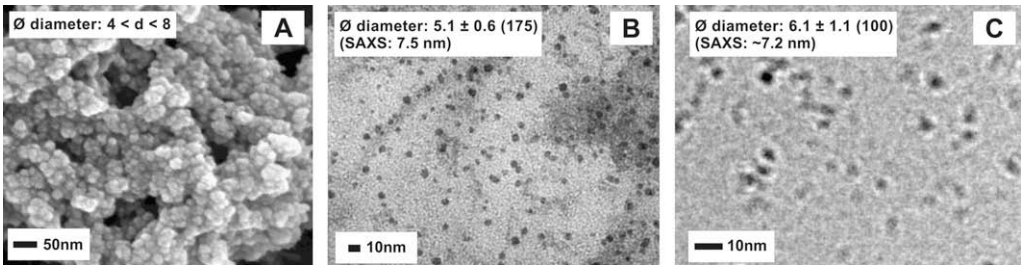

Fig. 7. (A) FEG–SEM and (B) TEM photomicrograph of silica nanoparticles grown for 30 min in a solution with 1600 ppm SiO_2 and IS of 0.22. (C) Cryo-TEM photomicrograph of silica nanoparticles quenched after 1.5 h from a solution with 1600 ppm SiO_2 and IS of 0.05.

Table 2
Comparison of particle diameters obtained from SAXS, DLS and TEM.

[$Si0_2$] (ppm)	IS	Time (h)	Particle diameter (nm)		
			SAXS[a]	DLS	TEM
640	0.02	1	5.8	4.6 ± 1.0	3.1 ± 0.4
		2	6.7	4.7 ± 1.1	3.3 ± 0.4
	0.11	1	7.0	—	—
		2	7.7	—	4.5 ± 0.7
	0.22	1	7.2	5.8 ± 1.9	5.2 ± 0.9
		2	8.0	8.0 ± 5.0	3.6 ± 0.5
1600	0.05	1	6.9	8.7 ± 2.2	—
		1.5	~7.2[b]	10.1 ± 3.1	6.1 ± 1.1[c]
		2	~7.5[b]	9.6 ± 1.8	—
	0.11	1	7.6	9.9 ± 3.5	5.4 ± 0.5
		2	7.9	Aggregation	—
	0.22	0.5	7.5	8.0 ± 1.0	5.1 ± 0.6
		1	7.9	Aggregation	6.7 ± 0.9
		2	7.9	Aggregation	—

[a] Error of SAXS <3%.
[b] Estimates based on the progression of growth curves obtained from SAXS.
[c] Result from cryo-TEM.

proaches, cryo-TEM photomicrographs of silica particles that were flash-frozen in solution in their native state from an experiment with 1600 ppm SiO_2 and IS = 0.05 were evaluated (Fig. 7C). The particle diameters obtained from cryo-TEM matched those derived from the SAXS measurements better than the results from conventional TEM (Table 2).

4.5. Kinetic analysis of SAXS data

The evaluation of the reaction kinetics of silica nanoparticle nucleation and growth was carried out with the time-resolved SAXS data from the experiments with 640 ppm SiO_2 and all three IS studied. The growth profiles of particles forming in higher concentrated solutions (1600 pm SiO_2) did not provide enough data points for a thorough kinetic analysis but they could be used for comparative qualitative analyses.

4.5.1. Nucleation

The fast decrease in monosilicic acid concentration (<5 min) when the pH of the experimental solutions was adjusted to 7 (Fig. 2) showed that silica polymerization was instantaneous. In addition, the lack of induction periods in SAXS data (i.e., particles were detected from the beginning of data collection) suggests that particle nucleation was instantaneous within the resolution of our study. This fits well with the goodness of fit of the SAXS data to the Chronomal kinetic model which assumes instantaneous, homogenous nucleation (Fig. 8).

Information on the radii of the critical nuclei, R_0, forming within the polymerizing solutions were obtained by extrapolation the particle growth profiles to $t = 0$ using the Chronomal analysis approach. R_0 values for all 640 ppm SiO_2 experiments are listed in Table 3 and vary between 1.09 and 1.00 nm with no apparent dependence on IS.

For comparison, critical nuclei sizes were also determined using the Gibbs–Kelvin equation (Gibbs, 1961, Table 3):

$$R_0^+ = 2v\sigma/R_cT\ln(S+1) \quad (9)$$

where v is the molar volume (27.2 cm^3; Iler, 1979), σ is the surface energy (for amorphous silica, 80 erg cm^{-2}; Iler, 1973), R_c, the gas constant, and S is the supersaturation defined as $S = (C - C_s)/C_s$ with C being the actual concentration and C_s the solubility (116 ppm SiO_2 at 25 °C; Gunnarsson and Arnórsson, 2000). In all 640 ppm SiO_2 experiments, the calculated R_0^+ values varied between

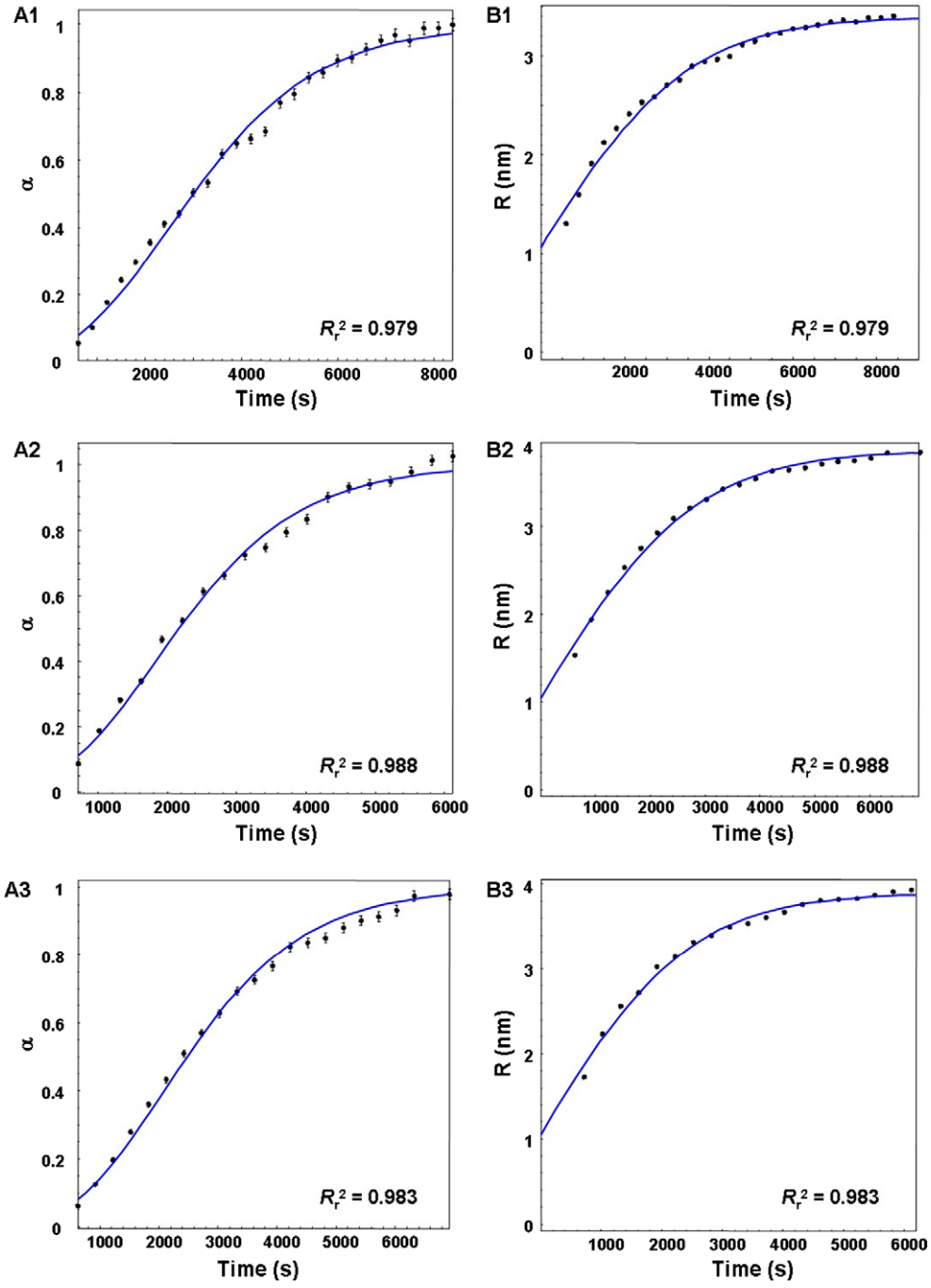

Fig. 8. Plots showing α (evaluated using Eq. (2); A1–A3) and *R* (evaluated from *R*g using Eq. (8); B1–B3) fits to the Chronomal model (solid line) for three SAXS experiments with 640 ppm SiO_2 and IS of 0.02 (A1 and B1), 0.11 (A2 and B2) and 0.22 (A3 and B3).

1.04 (IS = 0.22) and 1.07 (IS = 0.02) while in the 1600 ppm SiO_2 experiments, $R_0^+ = 0.67$–0.68 nm. Note that IS did not influence the critical nuclei radius substantially.

4.5.2. Growth mechanism: classical growth

In classical growth theory, particles grow by molecule-by-molecule attachment to a pre-existing surface. The growth profiles obtained from SAXS showed an initial fast and steady increase concomitant with the depletion of [SiO_2(aq)] to the point where saturation was almost reached and classical growth was no longer occurring. To test data from this initial growth phase, the SAXS data were fitted using two kinetic models, the Chronomal and the JMAK kinetics models, both of which are based on classical growth approaches.

Results from the Chronomal analysis for experiments with 640 ppm SiO_2 and IS = 0.02, 0.11 and 0.22 are shown in Fig. 8. Exceptionally good fits between the data and the

Table 3
Summary of the derived kinetic parameters. Critical nuclei radii, R_0^* were calculated from the Gibbs–Kelvin equation (Eq. (9)). An independent evaluation of the critical nuclei radii, R_0 along with the initial growth rate, G_0 were obtained from the Chronomal model. The Chronomal reaction constants, k were calculated using G_0 (Eq. (1)). Finally, the JMAK reaction constants, k^* were determined with the JMAK kinetic model (Eq. (7)).

[SiO_2] (ppm)	IS	R_0^+ (nm) Gibbs–Kelvin	Chronomal			JMAK
			[a]R_0 (nm)	G_0 ($\times 10^{-3}$ s^{-1})	k ($\times 10^{-4}$ s^{-1})	k^* ($\times 10^{-4}$ s^{-1})
640	0.02	1.07	1.09	0.70	5.13	2.77
	0.11	1.06	1.00	1.09	7.75	3.34
	0.22	1.04	1.05	1.20	8.22	3.61
[b]1600	0.05	0.68	—	—	—	—
	0.22	0.67	—	—	—	—

[a] Using R_0, an average interfacial surface energy of 77.9 ± 3.4 erg cm^{-2} was calculated.
[b] The 1600 ppm SiO_2 experiments did not provide enough data points for Chronomal and JMAK analysis.

kinetic model were obtained using a first order rate law with a surface-controlled mechanism (see R_r^2 values in Fig. 8). Chronomal fitting also provided an estimate for the initial growth rate, G_0, which was then used to calculate the rate constant, k (Eq. (1)). Values for both G_0 and k are listed in Table 3 and show an increase with increasing IS.

For comparison with the Chronomal analysis, the three different data sets were also fitted to the JMAK kinetic model (Fig. 9) and using the Avrami equation (Eq. (7)) an average exponent n of 1.7 ± 0.1 was obtained. The fit of the SAXS data with the JMAK model is reasonably good (Fig. 9) suggesting that the initial steps of silica nanoparticle growth proceed via classical growth. The rate constants, k^* determined from the JMAK analysis are given in Table 3. The data show that both the Chronomal and JMAK approach give k, respectively, k^* values of the same order of magnitude (10^{-4} s^{-1}), yet the Chronomal values (5.13–8.22 $\times$ 10^{-4} s^{-1}) are about twice as large compared to the values obtained from the JMAK fitting (2.77–3.61 $\times$ 10^{-4} s^{-1}).

4.5.3. Particle shape analysis

Some information about the structure and complexity of the particles could be derived by testing the SAXS data using a fractal geometry concept (Pfeifer and Obert, 1989; Lin et al., 1990). Boukari et al. (1997) employed the fractal geometry concept on alkoxide silica particle growth derived from SAXS patterns by analysing the power-law regime ($Rg^{-1} \ll q \ll a^{-1}$; where q is again the scattering vector and a is the size of the smallest unit building the fractal structure). In this regime, $I(q) \sim q^{-p}$, where the exponent p is related to the fractal dimension, D_f. For mass-fractals (D_m), which can be described as open, polymeric, low-density structures, $p = D_m$ with $1 < p < 3$ (3-D space) whereas surface-fractals (D_s) have uniform cores but open surface structures, $p = 6–D_s$ with $3 < p < 4$. The SAXS data from four experiments were least-square fitted with the power-law of $I(q) \sim q^{-p}$ with p being the fitting parameter. The changes of p over time are shown in Fig. 10.

The time evolution of p correlated well with the tested [SiO_2] and IS (i.e., the saturation state): higher saturated solutions (high [SiO_2]/high IS) induced fast changes in p while lower saturated solutions (low [SiO_2]/low IS) exhibited slower changes. Note that besides a shift in time, the trends of the p *vs.* time curves (Fig. 10) were identical for all fitted SAXS curves suggesting that the nucleation and growth processes did not change between experiments. Furthermore, despite a continuous change in particle structure as indicated by the increase in p, all formed particles can be described as mass-fractals ($1 < p < 3$; Fig. 10) and no transition to surface-fractal was observed. The observed inflection in the 1600 ppm SiO_2 experimental data is as yet unexplained and more work needs to be done to fully clarify these patterns. The data presented here however, are in agreement with previous studies on the early stages of silica nanoparticle formation prepared by the Stöber method (Boukari et al., 1997).

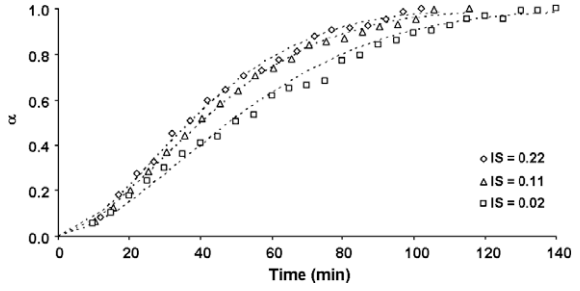

Fig. 9. Reaction process, α, with time for particle growth in polymerizing solutions with 640 ppm SiO_2 and IS of 0.02, 0.11 and 0.22. The dotted lines represent the fits to the JMAK kinetic model with n set to 1.7 and $t_0 = 0$ s.

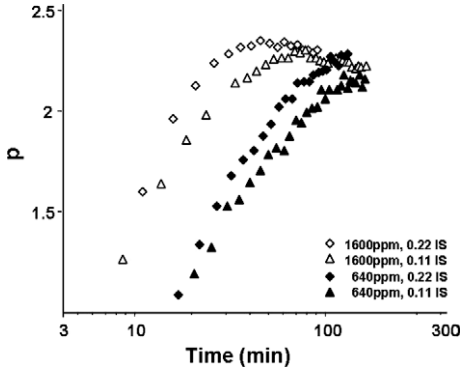

Fig. 10. Plot of exponent p determined from the power-law range of four SAXS profiles as a function of time.

4.5.4. Ostwald ripening and particle aggregation

Ostwald ripening (OR) has been suggested to be an important growth mechanism during the late stages of silica particle growth (Iler, 1979; Perry and Keeling-Tucker, 2000). The particle size information from the SAXS data was evaluated to determine if OR played a role in the final stages of silica nanoparticle formation. Lifshitz and Slyozov (1961) and Wagner (1961) independently derived theoretical expressions which are referred to as LSW theory. They described the coarsening of a precipitate (i.e., Ostwald ripening) due to the tendency to minimize the total particles surface free energy. According to the LSW theory, the mean particle radius follows a growth rate proportional to $t^{1/2}$ for interface kinetic limited growth, or proportional to $t^{1/3}$, for diffusion-limited growth. Plots representing the evolution of R *vs.* $t^{1/2}$ and $t^{1/3}$ are shown in Fig. 11. Note that the complete growth profiles (i.e., $0 < \alpha < 1$) are shown while the trendlines were only fitted to the later growth phases, which approximately fitted a linear trend. These plots show a minimal difference in the goodness of fit (Fig. 11, R_r^2 values) between the two different growth processes thus indicating that an OR model fit in this study fails to discriminate between a surface- ($t^{1/2}$) and diffusion controlled ($t^{1/3}$) mechanism (Fig. 11). The discrepancy between the OR model and the SAXS data indicates that it might be problematic to use the OR model as a growth mechanism for silica nanoparticles.

Besides an increase in mean particle radius, the LSW theory also states that during OR the particle size distribution broadens (i.e., increase in polydispersity) and its skewness changes to the left (Eberl et al., 1998). This was tested with the silica particle size distribution as determined for two different aging times (30 and 60 min) in a solution with 1600 ppm SiO_2 and IS of 0.22 using TEM photomicrographs (Fig. 12). The results show that at 30 min a fairly narrow size distribution (5.1 ± 0.6 nm, 200 particles measured) with almost Gaussian distribution was obtained. At 60 min, the size distribution broadened significantly (6.7 ± 0.9 nm, 200 particles measured) but no significant shift in skewness was observed (Fig. 12). Despite the absence of a shift in skewness, the increase in polydispersity could support OR, however this could also be indicative of particle aggregation.

Aggregation of monodisperse nanoparticles is generally described by two main models, diffusion-limited colloid aggregation (DLCA) and reaction-limited colloid aggregation (RLCA) (Weitz et al., 1985). Both DLS and SEM/TEM suggested the occurrence of particle aggregation (Figs. 6 and 7) within the latter stages of silica particle growth; however, these data sets did not provide enough data points for a thorough analysis of the aggregation mechanisms.

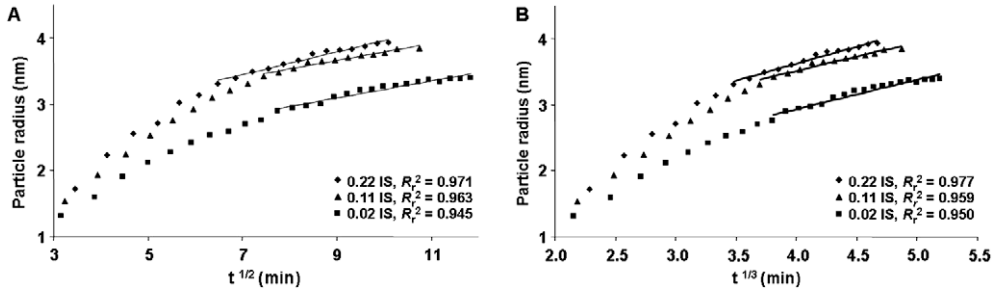

Fig. 11. Based on the LSW theory, the mean particle radius follows the growth rate proportional to (A) $t^{1/2}$ for interface kinetic limited growth or to (B) $t^{1/3}$, where growth is diffusion-limited.

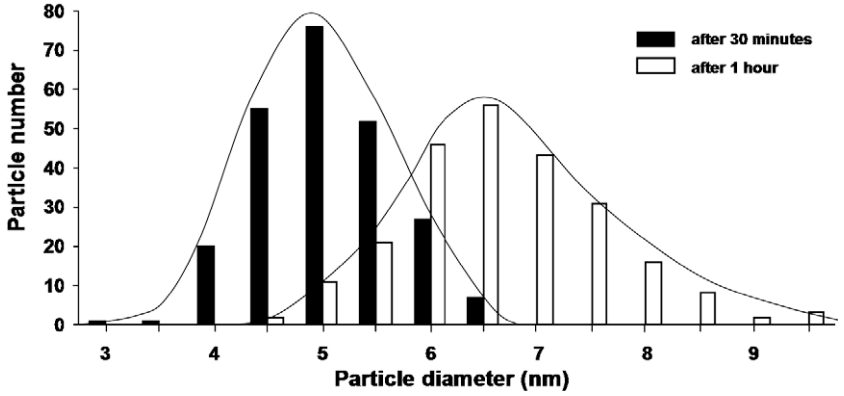

Fig. 12. Particle size distribution obtained from TEM photomicrographs of samples with 1600 ppm SiO_2 and IS = 0.22 for two different aging times.

5. DISCUSSION

All experiments were conducted at neutral pH and ambient room temperatures, where silica solubility is at a minimum (Iler, 1979). The SAXS and DLS results along with the time-dependent depletion of monosilicic acid confirmed previous studies that concluded that the rate of silica polymerization and nanoparticle formation increased with increasing ionic strength and silica concentration (Rothbaum and Rhode, 1979; Icopini et al., 2005; Conrad et al., 2007). In all experiments the reacting solutions were highly supersaturated with respect to amorphous silica and the degree of saturation invariably affected the growth rate and hence the time length of the reaction. In addition, due to the highly supersaturated state of the studied solutions, no induction periods were observed, i.e., silica polymerization occurred instantaneous (<5 min) during pH adjustment prior to data collection, suggesting that the first silica nanoparticles (critical nuclei) formed immediately after the initiation of the silica polymerization reaction. Note that the growth of silica nanoparticles (Fig. 4) appears to be more affected by IS than the time-dependent depletion of [SiO_2(aq)] (Fig. 2). This was not unexpected as the nucleation and growth of silica nanoparticles involves multiple steps (i.e., formation of dimers, trimers up to cyclic oligomers and polymers) and the reaction rate of each of these steps is slightly increased at higher IS thus resulting in a higher overall effect. In contrast, the time-dependent depletion of [SiO_2(aq)] only records the initial steps of silica polymerization (i.e., formation of dimers and trimers) and the effect of IS will thus not be as pronounced.

5.1. Particle size analysis

Particle growth curves obtained from SAXS showed that over 3 h the particle diameter increased from about 3 to 6 nm (depending on the concentration regimes) to a final diameter of ~8 nm (Fig. 4). The maximum size at the end of the initial growth phase were identical for all tested [SiO_2] and IS conditions and thus not affected by the degree of silica saturation. In contrast, the first particle size probed by SAXS differed significantly between experiments as a result of the different sized critical nuclei as well as the different growth rates, particularly in higher silica saturated solutions. Due to the experimental set-up the critical nuclei could not be probed directly by SAXS (first SAXS pattern collected after ~10 min of reaction) and therefore, the critical nuclei sizes were determined using the Chronomal approach and they were also calculated using the Gibbs–Kelvin approach (Table 3). The agreement between these values was very good and the comparison showed that in all solutions with 640 ppm SiO_2 the critical nuclei diameter was about 2 nm ($R_0 \sim 1$ nm, Table 3) with little influence of the tested IS. At higher silica concentrations (1600 ppm SiO_2), the critical nuclei size could only be determined via the Gibbs–Kelvin approach and these values were significantly smaller (~1.4 nm in diameter, $R_0 \sim 0.7$ nm, Table 3) than at lower [SiO_2]. The reason for this difference can stem from the fact that usually, the stability of the critical nuclei decreases with decreasing size (more energy is needed to sustain a higher surface to volume ratio; e.g., Lasaga, 1998) yet, the nucleation process has a higher driving force in more concentrated solutions thus enabling the stabilization of smaller critical nuclei. The values for the critical nuclei size obtained in this study were in good agreement with results from Iler (1979) who calculated that the first stable silica particle would range between 1 and 2 nm in diameter.

In Fig. 13, the direct comparison between the SAXS and DLS results for the growth of silica nanoparticles in a solution with 1600 ppm SiO_2 and IS of 0.05 are shown. Particularly in the initial stages of the reaction (<60 min) both growth curves follow the same trends, although the errors in the DLS data are substantially larger due to the lower accuracy of the DLS measurements at these small particle sizes. In both data sets the diameter of the first detected particle was ~4 nm. This was followed by a steady increase in particle diameter towards a final value of ~8 nm. After about 70 min, the DLS derived apparent mean particle diameter increased to sizes >15 nm (Fig. 13) while the SAXS and cryo-TEM data (at 60 and 90 min, respectively) showed final average particle diameters of 8 nm (see Fig. 4A, B) and 6 ± 1 nm, respectively (see Table 2). These differences are likely to be due to the formation of aggregates. In DLS, even 1–2% by volume of larger particles can significantly change the DLS derived particles size distribution while SAXS measurements are less susceptible to the presence of larger aggregates. Note that the formation of aggregates was also observed with SEM (Fig. 7A) while with TEM and cryo-TEM (Fig. 7B and C) only few aggregates were observed. However, it is likely that the aggregates observed with SEM/TEM were a consequence of sample preparation (i.e., dehydration) and therefore conventional SEM/TEM particle size measurements for silica nanoparticles do not provide a true picture of the proportion of the particles and aggregates within the suspension.

As shown in Table 2, the particle diameter obtained from SEM and (cryo-)TEM were generally smaller than those obtained from the DLS and SAXS data. The smaller mean particles diameters were not unexpected as for SEM and TEM analyses samples were imaged under high vacuum and thus they undergo dehydration and relaxation processes causing the highly hydrous (up to 13 wt% water; Krauskopf, 1956; Jones and Renaut, 2004) and open-structured silica particles to collapse. Particle diameters obtained from cryo-TEM (Table 2, Fig. 13) better matched the SAXS derived particle sizes

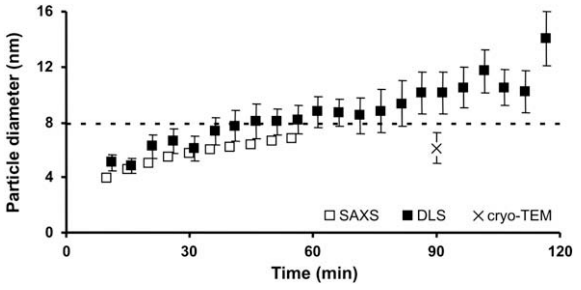

Fig. 13. Growth of silica nanoparticles as a function of time in a solution with 1600 ppm SiO_2 and IS of 0.05 measured by SAXS, DLS and cryo-TEM.

because the flash-frozen particles did not dehydrate within the high vacuum of the electron microscope. The observed difference (e.g., SAXS: 7.2 ± 0.3 and cryo-TEM: 6.1 ± 1.1) most likely resulted from the lower accuracy of determining sizes from cryo-TEM.

5.2. Analysis of the reaction kinetics

The initial stage of silica nanoparticle formation was characterized by silica polymerization where monosilicic acid coalescences to form dimers, trimers up to cyclic oligomers (Perry and Keeling-Tucker, 2000 and Fig. 2, initial 5 min). This polymerization process eventually led to the formation of stable nuclei having a diameter of approximately 1–2 nm (Table 3). Due to the dilute and highly supersaturated state of the silica solutions probed in this study (which enhances the diffusion of monosilicic acid to the forming nuclei), silica polymerization started immediately as the solutions were brought to the experimental conditions (i.e., pH = 7, first 5 min of reaction). This quasi-instantaneous initiation of the polymerization also warranted and justified that nucleation of silica nanoparticles occurred instantaneous (<5 min). This was further shown by the good fits of the SAXS data to the Chronomal model in which instantaneous nucleation was assumed.

The second step of silica nanoparticle formation was characterized by the fast decrease of [SiO_2(aq)] and the 3-D growth of silica nanoparticles. The dimensionality of the growth was shown by the Gaussian-shaped $p(R)$ curves as well as SEM and TEM photomicrographs which all indicated that the particles remained spherical throughout the reaction. Further evidence was provided by the quality of the fits to the Chronomal model (Fig. 8), which assumes 3-D growth and where the best fit in terms of the regression coefficient was obtained using a first order rate law with a surface-controlled mechanism. For a surface-controlled, 3-D growth mechanism, following a zero nucleation rate, the JMAK model should yield a n value of 3 (Hulbert, 1969). However, the n value calculated from the SAXS derived particle growth data was 1.7. Results from this study as well as from the literature (Iler, 1979; Icopini et al. 2005; Conrad et al., 2007) have shown that silica nanoparticles are spheres and n should therefore yield a value close to 3. This suggested that the use of the JMAK model for the growth of silica nanoparticle does not provide ideal fits. Similar problems were reported by Banfield and Zhang (2001) who concluded that although the JMAK theory can provide a general trend, it may not be suitable for analyses of reaction kinetics involving nano-phases and that rate constants derived from a JMAK approach should be interpreted with caution. This leads to the conclusion that the Chronomal model was more appropriate for the system studied and that the derived parameters and mechanisms are more accurate.

Nevertheless, the calculated rate constants, regardless of the kinetic model from which they were derived, showed similar values and trends (Table 3). In both models, the rate constant increased with increasing IS (i.e., increasing supersaturation), with the Chronomal rate constants being ~2 times larger than those obtained from the JMAK model. Rimstidt and Barnes (1980) obtained a rate constant of 2.7×10^{-4} s^{-1} using a first order kinetic model to describe silica precipitation (pH 7, $T = 25$ °C) which compares well with the values obtained in this study. Unfortunately, most other studies have used a reaction order >1 and the few that agreed on 1st order reaction kinetics differed in the reaction mechanisms (i.e., diffusion *vs.* surface-controlled mechanisms) making comparisons with other studies difficult. Furthermore, most previous studies followed the time-dependent decrease in monosilicic acid concentration, i.e., the silica polymerization process, and only inferred the reaction kinetics and mechanisms for silica nanoparticles growth. Despite silica polymerization and silica nanoparticle growth being intimately connected, they are two very different processes (chemically-controlled polymerization *vs.* 3-D, surface-controlled particle growth). Therefore, the reaction kinetics for the growth of silica nanoparticles cannot be derived from the kinetics of the initial silica polymerization process. This seems to be further complicated by the complexity of the silica polymerization process (e.g., dimerisation, oligomerisation) which to date is not well understood as indicated by the plethora of suggested reaction models for this process (Table 1). This supports the approach employed in this study where the reaction kinetics for silica nanoparticles formation was determined by following *in-situ* and time-resolved the nucleation and growth of silica nanoparticles in solution.

Ostwald ripening has been suggested by several studies to be involved in the process of silica nanoparticle growth. OR could not be inferred for the initial stages of particle growth, yet for the later stages of growth the close to linear trends observed in the R *vs.* $t^{1/2}$, $t^{1/3}$ plots (Fig. 11) and the increased polydispersity (Fig. 12) indicate a possible contribution of OR and/or particle aggregation (evidence from DLS; Fig. 6) to the growth process; specially in the stages of growth when the concentration of monosilicic acid approaches the solubility level and classical growth is energetically less favorable. However, the data did not allow a thorough discrimination between the possible contributions from OR or aggregation (see also later).

5.3. The structure of silica nanoparticles

Analysis of the power-law regime of SAXS profiles showed that the structure of the scattering particles was continuously changing (increase in p, Fig. 10) but that they were all mass-fractals, D_m ($p < 3$), characterized by polymeric, noncompact structures. This agrees well with previous studies (Iler, 1979; Perry and Keeling-Tucker, 2000) that have commented on the hydrous and porous structure of silica nanoparticles (the open nature of amorphous hydrated silica nanoparticles is well illustrated in Perry and Keeling-Tucker, 2000). It is not surprising, therefore that sample dehydration and exposure to high vacuum in the SEM and TEM measurements caused the particle structures to collapse, which explained the smaller particle sizes measured relative to SAXS, DLS and cryo-TEM (Table 2).

As shown in Fig. 10, p increased from ~1 to a final size of 2.2–2.3 for the tested suspensions. This steady increase was caused by the continuous hydrolysis of the growing particles, with hydroxyl groups being removed from the particles by in-

tra-particle densification/dehydration (Boukari et al., 1997). The establishment of the maximum p indicated the end of the densification process. Further growth of p to values >3 which would mark the transition from mass to surface-fractals (i.e., hydrolysis continues at the particle surface) was not observed. This is possibly a consequence of the short time scale probed in this study. Boukari et al. (1997) showed that depending on the saturation state of the solution as well as the physico-chemical conditions of the experiments the transition from open, polymeric structures to smooth silica nanoparticles can take hours to weeks. It is worth mentioning that previous studies (Avnir et al., 1998; Riello et al., 2003) have indicated that the power-law regime is often not wide enough for a good evaluation of the fractal particle structures. However, as indicated above, the fractal structures agreed well with observations from SEM and (cryo-) TEM and also compared well to values derived for silica particles produced by the Stöber method (Lin et al., 1990; Martin et al., 1990; Boukari et al., 1997).

5.4. Implications

Silica polymerization and the formation of silica nanoparticles are widespread in nature and occur in many terrestrial environments (e.g., geothermal waters, brines, seawater). Silica nanoparticles are also extensively used in industry and medicine where they can be produced by various methods to suit specific industrial applications. Regardless of the natural environment or the industrial application of silica nanoparticle formation, it is the size and structure of silica nanoparticles that determines their chemical and physical behavior (e.g., dissolution, adsorption, precipitation). Therefore, the information obtained in this study demonstrated for the first time that the final diameter of silica nanoparticles precipitated from supersaturated silica solutions (~8 nm) was more than double the sizes cited in the literature (~3–4 nm; e.g., Iler, 1979 and references therein, Icopini et al, 2005). This difference will undoubtedly affect the physico-chemical properties (e.g., specific surface area, chemical stability and reactivity) of the formed particles. Thus, energetic considerations and kinetic analyses of chemical and physical processes that involve silica nanoparticles need to be reconsidered in light of these new results.

6. SUMMARY

The time-dependent decrease of monosilicic acid concentration gave insight into the dynamics of silica polymerization, whereas *in-situ* time-resolved SAXS and DLS measurements provided the essential tools to monitor and quantify the initial steps of nucleation and growth of silica nanoparticles in aqueous solutions. SEM and TEM verified the results obtained by SAXS and DLS providing snap-shots of particle size and shape at specific time steps during the reaction.

Overall, from the data presented above it can be concluded that the nucleation and growth of silica nanoparticle is governed by a series of processes driven and controlled by various kinetic mechanisms. These processes can be divided into three main stages (Fig. 14):

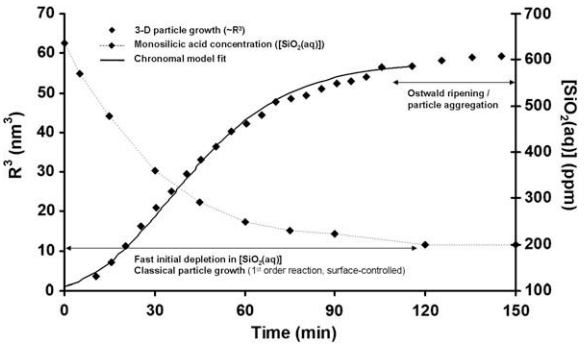

Fig. 14. Schematic illustration of the growth stages of silica nanoparticles from supersaturated solutions. Instantaneous homogeneous nucleation occurs at $t = 0$ min, followed by initial fast particle growth ($\sim R^3$) concomitant with the decrease in [SiO_2(aq)], and by particle aggregation/Ostwald ripening at longer time scales.

(1) Nucleation stage: characterized by instantaneous homogeneous nucleation where monosilicic acid polymerizes to form stable critical nuclei having a diameter of approximately 1–2 nm;

(2) 3-D growth stage: characterized by silica nanoparticle growth following first order reaction kinetics coupled with a surface-controlled reaction mechanism;

(3) Ostwald ripening/aggregation stage: the 3-D classical growth ends and Ostwald ripening and particle aggregation set in.

Stages (1) and (2) are also mirrored by the fast decrease of monosilicic acid concentration while during stage (3), [SiO_2 (aq)] approaches solubility levels.

At the end of this 3-stage process, regardless of the tested silica concentration and ionic strength, the final silica nanoparticles were about 8 nm in diameter and characterized by mass fractal structure (i.e., open, polymeric structure).

ACKNOWLEDGMENTS

The authors thank Wim Bras and the station scientists from the Dutch–Belgian beamline (DUBBLE) at the European Synchrotron Radiation Facility (ESRF), Grenoble, France, for beamtime and technical assistance. We also specifically thank Mike Hounslow (Chemical and Process Engineering, University of Sheffield, UK) for help and guidance of how to use the Chronomal approach for the evaluation of our SAXS data and for explaining the mathematical background behind this kinetic model. D.J.T. acknowledge John Harrington, Adrian Hick and David Parcej for their assistance with FEG–SEM, TEM and cryo-TEM work, respectively. Many thanks also to Susanne Patel and Jennifer Green from Particles CIC (University of Leeds, UK) for help with DLS logistics. Financial support via a PhD fellowship for DJT from the Earth and Biosphere Institute (University of Leeds, UK), and research funds for LGB from the University of Leeds are acknowledged. The authors thank the three anonymous reviewers for their valued comments.

REFERENCES

Alexander G. B. (1954) The polymerization of monosilicic acid. *J. Am. Chem. Soc.* **76**, 2094–2096.

Avrami M. (1939) Kinetics of phase change, I. *J. Chem. Phys.* **7**, 1103–1112.

Avrami M. (1940) Kinetics of phase change, II. *J. Chem. Phys.* **8**, 212–224.

Avnir D., Biham O., Lidar D. and Malcai O. (1998) Applied mathematics: is the geometry of nature fractal? *Science* **279**, 39–40.

Bailey J. K. and Mecartney M. L. (1992) Formation of colloidal silica particles from alkoxides. *Colloids Surf.* **63**, 151–161.

Ball J. W. and Nordstrom D. K. (1992) *Geochemical model to calculate speciation of major, trace and redox elements in natural waters*. U.S. Geological Survey, International Groundwater Modeling Centre.

Banfield J. F. and Zhang H. (2001) Nanoparticles in the environment. In *Reviews of Mineralogy and Geochemistry* (eds. J. F. Banfield and A. Navrotsky). Mineralogical Society of America, Washington, DC, pp. 1–58.

Barghorn E. S. and Tyler S. A. (1965) Microorganisms from the gunflint chert. *Science* **147**, 563–577.

Baumann H. (1959) Polymerization und Depolymerization der Kieselsäure unter verschiedenen Bedingungen. *Kolloid Z.* **162**, 28–35.

Benning L. G., Phoenix V. and Mountain B. W. (2005) Biosilicification: the role of cyanobacteria in silica sinter deposition. In *Micro-organisms and earth systems: advances in geomicrobiology* (eds. G. M. Gadd, K. T. Semple and H. M. Lappin-Scott). SGM Symposium, Cambridge University Press. pp. 131–150.

Bishop A. D. and Bear J. L. (1972) The thermodynamics and kinetics of the polymerization of silicic acid in dilute aqueous solutions. *Thermochim. Acta* **3**, 399–409.

Borsboom M., Bras W., Crejak I., Detollenaere D., Glastra van Loon D., Goedtkindt P., Konijnenburg M., Lassing P., Levine Y. K., Munneke B., Oversluizen M., van Tol R. and Vlieg E. (1998) The Dutch–Belgian beamline at the ESRF. *J. Synchrotron Radiat.* **5**, 518–520.

Bogush G. H., Tracy M. A. and Zukoski IV C. F. (1988) Preparation of monodisperse silica particles: controls of size and mass fraction. *J. Non-Cryst. Solids* **104**, 95–106.

Boukari H., Lin J. S. and Harris M. T. (1997) Probing the dynamics of the silica nanostructure formation and growth by SAXS. *Chem. Mater.* **9**, 2376–2384.

Boukari H., Long G. G. and Harris M. T. (2000) Polydispersity during formation and growth of the Stöber silica particles from Small-Angle X-Ray Scattering measurements. *J. Colloid Interface Sci.* **229**, 129–139.

Bras W., Dolbnya I. P., Detollenaere D., van Tol R., Malfois M., Greaves G. N., Ryan A. J. and Heeley E. (2003) Recent experiments on a combined small-angle/wide-angle X-ray scattering beam line at the ESRF. *J. Appl. Cryst.* **36**, 791–794.

Carroll S., Mroczek E., Alai M. and Ebert M. (1998) Amorphous silica precipitation (60 to 120 °C): comparison of laboratory and field rates. *Geochim. Cosmochim. Acta* **62**, 1379–1396.

Carson G. A. (1991) Silicification of fossils. In *Taphonomy, Releasing the Data Locked in the Fossil Record* (eds. P. A. Allison and D. E. G. Briggs). Plenum Press, New York, pp. 455–499.

Conrad C. F., Yasuhara H., Bandstra J. Z., Icopini G. A., Brantley S. L. and Heaney P. J. (2007) Modeling the kinetics of silica nanocolloid formation and growth in aqueous solutions as a function of pH and ionic strength. *Geochim. Cosmochim. Acta* **71**, 531–542.

Crerar D., Axtmann E. V. and Axtmann R. C. (1981) Growth and ripening of silica polymers in aqueous solutions. *Geochim. Cosmochim. Acta* **45**, 1259–1266.

Eberl D. D., Drits V. A. and Srodon J. (1998) Deducing growth mechanisms for minerals from the shapes of crystal size distributions. *Am. J. Sci.* **298**, 499–533.

Egelhaaf S. U., Schurtenberger P. and Müller M. (2000) New controlled environment vitrification system for cryo-transmission electron microscopy: design and application to surfactant solutions. *J. Microsc.* **200**, 128–139.

Gibbs W. (1961) *The Scientific Papers*, *vol. I*. Dover Publications, Inc., New York.

Glatter O. and Kratky O. (1982) *Small Angle X-ray Scattering*. Academic Press, New York.

Goto K. (1956) Effect of pH on polymerization of silicic acid. *J. Phys. Chem.* **60**, 1007–1008.

Green D. L., Lin J. S., Lam Y.-F., Hu M. Z.-C., Schafer D. W. and Harris M. T. (2003a) Size, volume fraction, and nucleation of Stöber silica nanoparticles. *J. Colloid Interface Sci.* **266**, 346–358.

Green D. L., Jayasundara S., Lam Y.-F. and Harris M. T. (2003b) Chemical reaction kinetics leading to the first Stöber silica nanoparticles–NMR and SAXS investigation. *J. Non-Cryst. Solids* **315**, 166–179.

Greenberg A. E., Trussell R. R. and Clesceri L. (1985) *Standard Methods for the Examination of Water and Wastewater*. American Public Health Association, New York.

Guidry S. A. and Chafetz H. S. (2002) Factors governing subaqueous siliceous sinter precipitation in hot springs: examples from Yellowstone National Park, USA. *Sedimentology* **49**, 1253–1267.

Guinier A. (1939) La diffraction des rayons X aux tres petits angles: application a l'étude de phénomenes ultramicroscopiques. *Ann. Phys.* **12**, 161–237.

Gunnarsson I. and Arnórsson S. (2000) Amorphous silica solubility and the thermodynamic properties of H_4SiO_4 in the range of 0 to 350 °C at Psat. *Geochim. Cosmochim. Acta* **64**, 2295–2307.

Gunnarsson I. and Arnórsson S. (2003) Silica scaling: the main obstacles in efficient use of high-temperature geothermal fluids. *Int. Geoth. Conf. Reykjavik* **3**, 30–36.

Hinman N. W. (1990) Chemical factors influencing the rates and sequences of silica phase transitions: effects of organic constituents. *Geochim. Cosmochim. Acta* **54**, 1563–1574.

Hulbert S. F. (1969) Models for solid-state reactions in powered compacts: a review. *J. Br. Ceram. Soc.* **6**, 11–20.

Icopini G. A., Brantley S. L. and Heaney P. J. (2005) Kinetics of silica oligomerization and nanocolloid formation as a function of pH and ionic strength at 25 °C. *Geochim. Cosmochim. Acta* **69**, 293–303.

Iler R. K. (1973) Colloidal silica. In *Surface and Colloid Science* (ed. E. Matijevic). Wilery Interscience & Plenum Publisher.

Iler R. K. (1979) *The Colloid Chemistry of Silica and Silicates*. Cornell University Press, Ithaca, New York.

Johnson P. F. and Mehl R. F. (1939) Reaction kinetics in processes of nucleation and growth. *A. I. M. E. Tech. Pubs.* **1089**, 1–27.

Jones B. and Renaut R. W. (2004) Water content of opal-A: implications for the origin of laminae in Geyserite and sinter. *J. Sediment. Res.* **74**, 117–128.

Kitahara S. (1960) The polymerization of silicic acid obtained by the hydrothermal treatment of quartz and the solubility of amorphous silica. *Rev. Phys. Chem. Jpn.* **30**, 131–137.

Knoll A. H. (1985) Exceptional preservation of photosynthetic organisms in silicified carbonates and silicified peats. *Philos. Trans. R. Soc. Lond.* **311**, 11–122.

Konhauser K. O., Jones B., Phoenix V. R., Ferris F. G. and Renaut R. W. (2004) The microbial role in hot spring silicification. *Ambio* **33**, 552–558.

Krauskopf K. B. (1956) Dissolution and precipitation of silica at low temperatures. *Geochim. Cosmochim. Acta* **10**, 1–26.

Lasaga A. C. (1998) *Kinetic Theory in the Earth Sciences*. Princeton University Press, Princeton, New Jersey.

Lifshitz I. M. and Slyozov V. V. (1961) The kinetics of precipitation from supersaturated solid solutions. *J. Phys. Chem. Solids* **19**, 35–50.

Lin M. Y., Lindsay H. M., Weitz D. A., Ball R. C., Klein R. and Meakin P. (1990) Universal reaction-limited colloid aggregation. *Phys. Rev. A* **41**, 2005–2020.

Makrides A. C., Turner M. J., Harvey W. W., Slaughter J., Brummer S. B., Offenhartz P. O'D. and Pearson G. F. (1977) *Study of silica scaling from geothermal brines*. Master thesis, U.S. Department of Energy.

Makrides A. C., Turner M. and Slaughter J. (1980) Condensation of silica from supersaturated silicic acid solutions. *J. Colloid Interface Sci.* **73**, 345–367.

Marshall W. L. and Warakomski J. M. (1980) Amorphous silica solubilities–II. Effect of aqueous salt solutions at 25 °C. *Geochim. Cosmochim. Acta* **44**, 915–924.

Marshall W. L. and Chen C.-T. A. (1982) Amorphous silica solubilities – V. Predictions of solubility behaviour in aqueous mixed electrolyte solutions to 300 °C. *Geochim. Cosmochim. Acta* **46**, 289–291.

Martin J. E., Wilcoxon J. P., Schaefer D. and Odinek J. (1990) Fast aggregation of colloidal silica. *Phys. Rev. A* **41**, 4379–4391.

Matsoukas T. and Gulari E. (1988) Dynamics of growth of silica particles from ammonia-catalyzed hydrolysis of tetra-ethyl-orthosilicate. *J. Colloid Interface Sci.* **124**, 252–261.

Mountain B. W., Benning L. G. and Boerema J. (2003) Experimental studies on New Zealand hot spring sinters: rates of growth and textural development. *Can. J. Earth Sci.* **40**, 1643–1667.

Nielsen A. E. (1964) Kinetics of precipitation. In *International Series of Monographs on Analytical Chemistry* (eds. R. Belcher and L. Gordon). Pergamon Press, Oxford, UK.

Okamoto G., Okura T. and Goto K. (1957) Properties of silica in water. *Geochim. Cosmochim. Acta* **12**, 123–132.

Parkhurst D. L. and Appelo C. A. J. (1999) *User's guide to PHREEQC (version 2)-A computer program for speciation, batch-reaction, one-dimensional transport, and inverse geochemical calculations.* US Geological Survey, Water-Resources Investigations Report.

Peck L. B. and Axtmann R. C. (1979) A theoretical model of the polymerization of silica in aqueous media. Int. Symp. on Oilfield and Geothermal Chemistry, *Soc. Pet. Eng. A.I.M.E. Trans.*, pp. 239–247.

Perry C. C. and Keeling-Tucker T. (2000) Biosilicification: the role of the organic matrix structure control. *J. Biol. Inorg. Chem.* **5**, 537–550.

Perry C. C. (2003) Biosilicification: structure, regulation of structure and model studies. In *Silicon Chemistry – From Molecules to Extended Systems* (eds. P. Jutzi and U. Schubert). Weinheim, Wiley-VCH.

Pfeifer P. and Obert M. (1989) Fractals: basic concepts and terminology. In *The Fractal Approach to Heterogeneous Chemistry: Surfaces, Colloids, Polymers* (ed. D. Avnir). Wiley, New York.

Pontoni D., Narayanan T. and Rennie A. R. (2002) Time-resolved SAXS study of nucleation and growth of silica colloids. *Langmuir* **18**, 56–59.

Riello P., Minesso A., Craievich A. and Benedetti A. (2003) Synchrotron SAXS study of the mechanisms of aggregation of sulfate zirconia sols. *J. Phys. Chem. B* **107**, 3390–3399.

Rimstidt J. D. and Barnes H. L. (1980) The kinetics of silica–water reactions. *Geochim. Cosmochim. Acta* **44**, 1683–1699.

Rothbaum H. P. and Rhode A. G. (1979) Kinetics of silica polymerization and deposition from dilute solutions between 5 and 180 °C. *J. Colloid Interface Sci.* **71**, 533–559.

Rothbaum H. P. and Wilson R. D. (1977) Effect of temperature and concentration on the rate of polymerization of silica in geothermal waters. In *Geochemistry 1977*. New Zealand Dept. Sci. Ind. Res. Bull.

Squyres S. W., Arvidson R. E., Ruff S., Gellert R., Morris R. V., Ming D. W., Crumpler L., Farmer J. D., Des Marais D. J., Yen A., McLennan S. M., Calvin W., Bell, III, J. F., Clark B. C., Wang A., McCoy T. J., Schmidt M. E. and a Jr P. A. (2008) Detection of silica-rich deposits on mars. *Science* **320**, 1063–1067.

Stöber W., Fink A. and Bohn E. (1968) Controlled growth of monodisperse silica spheres in the micron size range. *J. Colloid Interface Sci.* **26**, 62–69.

Svergun D. I. (1992) Determination of the regularization parameter in indirect-transform methods using perceptual criteria. *J. Appl. Cryst.* **25**, 495–503.

Svergun D. I. and Koch M. H. J. (2003) Small-angle scattering studies of biological macromolecules in solution. *Rep. Prog. Phys.* **66**, 1735–1782.

Van Blaaderen A., van Geest J. and Vrij A. (1992) Monodisperse colloidal silica spheres from tetraalkoxysilanes: particle formation and growth mechanism. *J. Colloid Interface Sci.* **154**, 481–501.

Wagner C. (1961) Theorie der Alterung von Niderschlagen durch Umlosen (Ostwald Reifung). *Z. Electrochem.* **65**, 581–591.

Weitz D. A., Huang J. S., Lin M. Y. and Sung J. (1985) Limits of the fractal dimension for irreversible kinetic aggregation of gold colloids. *Phys. Rev. Lett.* **54**, 1416–1419.

Weres O., Yee A. and Tsao L. (1981) Kinetics of silica polymerization. *J. Colloid Interface Sci.* **84**, 379–402.

Westall F. and Walsh M. M. (2000) The diversity of fossil microorganisms in Archaen-age rocks. In *Journey to Diverse Microbial Worlds* (ed. J. Seckbach). Kluwer, Amsterdam.

White D. E., Brannock W. W. and Murata K. J. (1956) Silica in hot spring waters. *Geochim. Cosmochim. Acta* **10**, 27–59.

Williams L. A. and Crerar D. A. (1985) Silica diagenesis II. General mechanisms. *J. Sediment. Petrol.* **55**, 312–321.

Associate editor: Jon Chorover